NANO LETTERS
Letter
Cite This: Nano Lett. 2019, 19, 576–581
pubs.acs.org/NanoLett

Electron Transport in Nanoporous Graphene: Probing the Talbot Effect

Gaetano Calogero,*[,†] Nick R. Papior,[†] Bernhard Kretz,[‡] Aran Garcia-Lekue,[§,∥] Thomas Frederiksen,[§,∥] and Mads Brandbyge*[,†]

[†]Department of Micro- and Nanotechnology, Center for Nanostructured Graphene (CNG), Technical University of Denmark, DK-2800 Kongens Lyngby, Denmark

[‡]Institute of Theoretical Physics, University of Regensburg, 93040 Regensburg, Germany

[§]Donostia International Physics Center (DIPC), 20018 San Sebastian, Spain

[∥]Ikerbasque, Basque Foundation for Science, 48013 Bilbao, Spain

Supporting Information

ABSTRACT: Electrons in graphene can show diffraction and interference phenomena fully analogous to light thanks to their Dirac-like energy dispersion. However, it is not clear how this optical analogy persists in nanostructured graphene, for example, with pores. Nanoporous graphene (NPG) consisting of linked graphene nanoribbons has recently been fabricated using molecular precursors and bottom-up assembly (Moreno et al. *Science* **2018**, *360*, 199). We predict that electrons propagating in NPG exhibit the interference Talbot effect, analogous to photons in coupled waveguides. Our results are obtained by parameter-free atomistic calculations of real-sized NPG samples based on seamlessly integrated density functional theory and tight-binding regions. We link the origins of this interference phenomenon to the band structure of the NPG. Most importantly, we demonstrate how the Talbot effect may be detected experimentally using dual-probe scanning tunneling microscopy. Talbot interference of electron waves in NPG or other related materials may open up new opportunities for future quantum electronics, computing, or sensing.

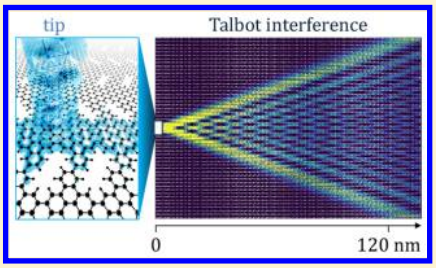

KEYWORDS: *Nanoporous graphene, Talbot interference, electron transport, scanning probe microscopy, multiscale modeling*

Controlling electron waves by harnessing phase-coherence and interference effects is a cornerstone for future nanoelectronics,[1,2] quantum computing,[3] sensing,[4] or electron beam splitting.[5] To this end, design of platforms with well-defined, narrow, and low-loss propagation channels is essential.

Nanoporous graphene (NPG) holds great potential for distributing and controlling currents on the nanoscale.[6,7] By achieving bottom-up synthesis and transfer of atomically precise NPGs, Moreno et al.[8] have recently paved the way for the fabrication of high-quality NPG-based devices. Further functionalization or engineering of the pore edges could offer additional opportunities to manipulate electron transport.[9] The particular edge topology of the linked graphene nanoribbons (GNRs) making up the NPG results in a pronounced in-plane anisotropy, which is reflected in the electronic structure as a peculiar energy-dependent 1D localization of electron states near the conduction band. Two-terminal electrical measurements and simulations successfully proved the semiconducting nature of NPG and the anisotropic electron propagation within the mesh.[8] However, the fixed electrode setup did not answer the question of how transmitted electrons are confined in a single GNR and whether 1D directed electron flow is possible. Moreover, it is unclear to what extent the typical optics analogy used for electron transport in pristine graphene devices[10−13] can work for devices based on NPG.

Visualizing current flow in NPG represents the most direct route to tackle these questions in an experiment. Several techniques based on superconducting interferometry,[14,15] scanning gate microscopy,[16] or diamond nitrogen-vacancy centers[17] have demonstrated how imaging real-space current flow in graphene structures can profitably underpin standard electrical measurements for classical or quantum-transport phenomena, whereas scanning probe spectroscopies are now proving to be able to probe these currents on the atomic scale.[18]

In this Letter, we theoretically investigate to what extent one can inject currents along individual GNR channels in gated NPG-based devices contacted chemically to a scanning tunneling microscope (STM) probe. We develop a multiscale method based on density functional theory (DFT) and non-equilibrium Green's functions (NEGF), enabling current calculations with devices longer than 100 nm, relevant for experiments. This is accomplished by linking a perturbed contact region described by DFT to an unperturbed large-scale region described by an effective tight-binding (TB) model parametrized from DFT. We find that the inter-GNR coupling

Received: November 15, 2018
Revised: December 11, 2018
Published: December 12, 2018

DOI: 10.1021/acs.nanolett.8b04616
Nano Lett. 2019, 19, 576–581

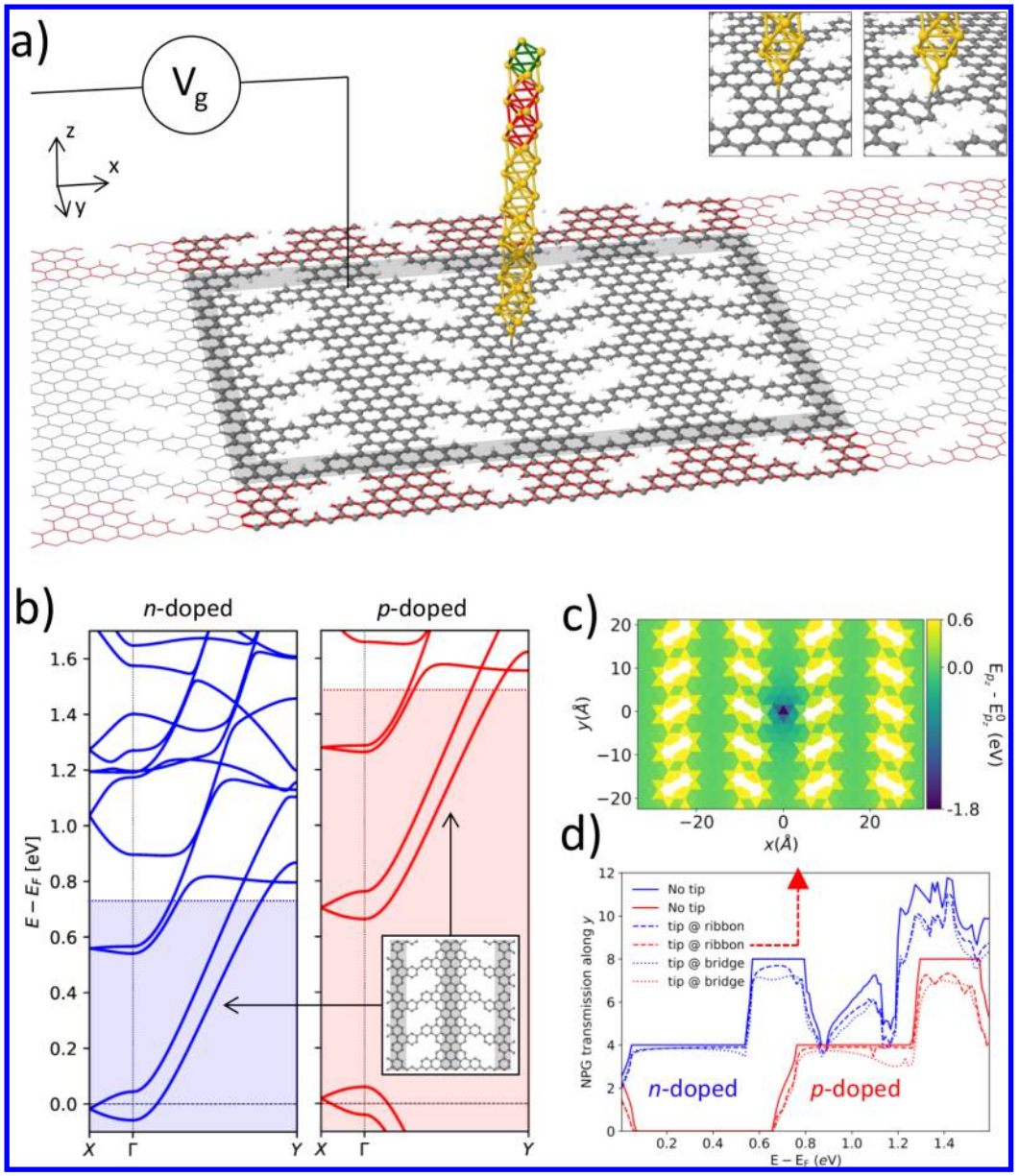

Figure 1. DFT model of NPG. (a) DFT model of gated NPG-based device with contact to STM tip. Electrodes are highlighted in red. Insets show the optimized contact regions for ribbon and bridge positions. The shaded area delimits the device region. (b) Band structure of the NPG unit cell under two gated conditions inducing either n-type (blue, $n_g = +10^{13}\ e^-\ cm^{-2}$) or p-type (red, $n_g = -10^{13}\ e^-\ cm^{-2}$) doping. States with energies in the shaded areas, that is, up to ∼0.7 eV above (below) the conduction (valence) band, disperse more along Γ−*Y* than along Γ−*X*, hence defining predominantly longitudinal transport channels. (c) On-site potential of C p_z orbitals in a p-doped NPG. Values are relative to the average potential E^0_{pz} in the bulk of ribbons ∼0.5 nm away from the tip. Beyond this distance, the perturbation from the tip is effectively screened. (d) Transmission between the two NPG electrodes, with and without tip contact, for the two different tip positions in panel a and gated conditions in panel b.

disrupts the longitudinal electron confinement into individual channels, giving rise to the Talbot effect, a fascinating interference phenomenon predicted to occur in discrete optical waveguide systems.[19−24] The fine detail of Talbot wave interference is the origin of various technological applications, ranging from lithography[25] to phase-contrast interferometry.[26] Besides, it was predicted to occur for massless Dirac Fermions in graphene[23] as well as plasmons in single-mode GNRs arrays.[24] We prove the robustness of the electronic Talbot effect in NPG by injecting current from the STM tip into various NPG sites and under various gating conditions. Using proof-of-principle calculations, we also predict how this effect can be detected using a second STM tip.

We carry out transport calculations based on NEGF[27−29] applied to DFT or TB models using TranSIESTA,[30,31] TBtrans,[31] and SISL.[32] Whereas parameter-free DFT models limit the accessible device sizes to only a few nanometers, parametrized TB can capture basic transport features of large systems with minor chemical perturbations (e.g., metal contact or chemical hybridization). The DFT model for the NPG device, shown in Figure 1a, covers an area of 6.5 × 5.5 nm^2 (1449 atoms), and it is defined on a single-ζ polarized basis set. This choice guarantees enough accuracy over an energy range of ∼±2 eV from E_F. A better basis would be needed to capture superatom bands at $E - E_F > 2$ eV.[8,33] We use the GGA-PBE exchange-correlation functional[34] and open (periodic) boundary conditions along *y* (*x*) while sampling the *x* direction with

DOI: 10.1021/acs.nanolett.8b04616
Nano Lett. 2019, 19, 576−581

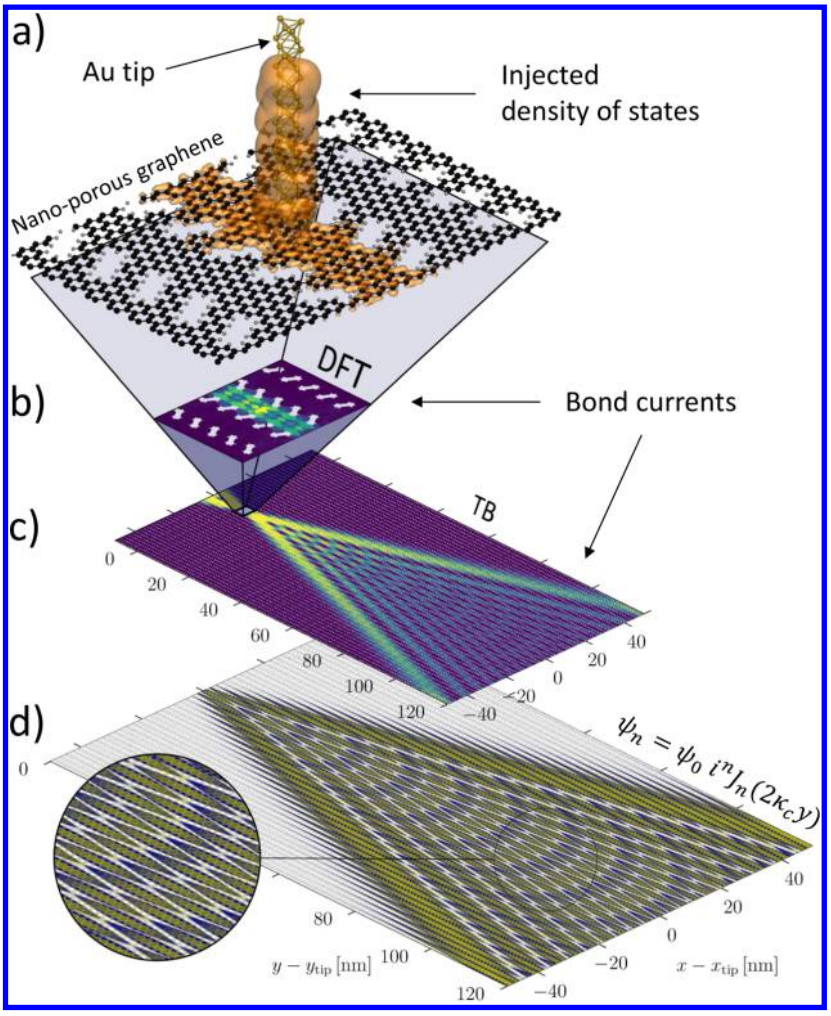

Figure 2. Talbot effect from multiscale calculations of n-doped NPG. (a) DFT geometry and density of states injected by the tip, (b) bond currents at $E - E_F = 0.2$ eV obtained with the DFT model, (c) a large-scale TB model with DFT-precision injection region, and (d) the best-fit to the Talbot effect equations. In panel d, the local spectral density of states (ADOS) from the tip is shown in yellow, scaled by $y - y_{tip}$ to compensate damping occurring far from the tip. The fitted equations ψ_n are plotted in blue underneath the ADOS. The integers $n \in [-26,26]$ index the 53 GNR rows along the y direction (covering a width of 100 nm across the x axis).

5 k-points. Pores are passivated with H atoms, and a model Au tip is in chemical contact with the NPG. The tip structure is chosen so as to ensure a flat local density of states on the tip apex over the range $[-0.75, 1\ \text{eV}]$, relevant for our study. The coordinates of the tip apex and up to 20 C atoms nearby are optimized until forces are <0.01 eV/Å. After the optimization, the Au−C bond length is ∼2.0 Å. To describe a more realistic experimental environment, we self-consistently include a bottom gate in the calculations. This is done by fixing spatial charge in a gate-layer placed 15 Å beneath the NPG, so as to dope it by $n_g = \pm 10^{13}\ e^-\ \text{cm}^{-2}$.[35] The device Green's function is calculated as

$$\mathbf{G} = \left[\mathbf{S}(E + i\eta) - \mathbf{H} - \sum_i \mathbf{\Sigma}_i\right]^{-1} \quad (1)$$

where $\mathbf{S}$ and $\mathbf{H}$ are the model overlap and Hamiltonian and $\mathbf{\Sigma}_i$, called self-energy, connects the device to semi-infinite regions along x (electrodes). A self-energy allows us to seamlessly connect different regions, be it infinite bulk or localized perturbations. We exploit this to embed one or more DFT-precision regions inside much larger TB models, which are needed to reach experimental relevant dimensions and observe interference. The central idea of this multiscale approach is to construct the self-energy connecting p_z orbitals of the outermost unperturbed DFT atoms (shaded frame in Figure 1a) to a larger p_z TB model. We obtain TB parameters from a DFT calculation of unperturbed NPG such that the resulting model retains the interaction range of the DFT basis set, is nonorthogonal, and takes the self-consistent effects of gates or bias into account. Therefore, besides introducing local DFT precision in the TB model, this method enables TB-based N-electrode transport calculations without any fitting parameters. We refer to the Supporting Information for details of the DFT calculations and the multiscale method.

We consider two different positions of the tip, namely, on top of a C atom in the middle of a ribbon or at a bridge between two C atoms linking two ribbons (see the inset to Figure 1a). In the former case, the C atoms below the tip are pushed ∼0.3 Å below the NPG plane, whereas at the bridge site the tip binds to two aromatic rings, causing a slight torsion.

The main effect of gating on the NPG electronic structure is a rigid band shift of ±0.35 eV for n- and p-type doping, respectively (Figure 1b). We find in both cases a band gap of

DOI: 10.1021/acs.nanolett.8b04616
Nano Lett. 2019, 19, 576−581

~0.7 eV between symmetric valence and conduction bands, in good agreement with results obtained for nongated NPG.[8] Bands with predominant longitudinal character are clearly visible at energies up to 0.7 to 0.8 eV above (below) the conduction (valence) band (shaded areas), where states along $\Gamma-Y$ indeed disperse more than those along $\Gamma-X$. The contact with the tip causes local variation of the C p_z potential, which is screened at ~0.5 nm from the tip (Figure 1c). This degrades transmission between the two NPG electrodes along the y direction (Figure 1d). For all energies in the longitudinal regime, transport is essentially 1D along the GNRs due to the weak inter-ribbon coupling. The onset at $E \approx 0.9$ eV of bands with dominant transverse character disrupts the 1D confinement, and conductance quantization is lost.

For both n- and p-type NPG and both tip positions, we find qualitatively similar electronic and transport features (see Figures S1 and S2). Therefore, without loss of generality, we focus in the following on the n-doped NPG case probed at the ribbon site.

We visualize the electron flow near the contact through the injected density of states (injected density of states is calculated by summing the absolute modules of the three eigenchannels,[36] which contribute the most to transmission from the tip to the NPG electrodes) and bond currents from the tip (bond currents are defined as $J_{\alpha\beta} = \sum_{\nu\in\alpha}\sum_{\mu\in\beta} J_{\nu\mu}$, where ν (μ) indicates a basis orbital centered on atom α (β)), as shown in Figure 2a,b. These clearly demonstrate electron confinement inside the probed ribbon up to distances comparable to the DFT cell size for all energies ranging from the conduction band up to ~0.7 eV above it (see Figure S2). We study the distribution of electronic current in the far-field, that is, far from the source, by performing transport calculations where the DFT "injection region" is embedded into a larger TB NPG model. We benchmark the applicability of this method by embedding the DFT-precision injection region in a TB region that has the same boundary conditions and size of the DFT transport setup (see Figure S4). The results show that we can reproduce the DFT transmission spectra in the longitudinal regime (Figure 1b, shaded) by the combined DFT+TB model.

Next, we embed the DFT injection region as an electrode in a large 100 nm × 120 nm TB model of a device with two NPG electrodes along y and a complex absorbing potential[37,38] along x. This larger model reveals that at distances beyond the DFT cell size, transversal losses significantly affect the far-field behavior (Figure 2c). Current splits into neighboring ribbons with a certain periodicity of ~7 to 8 nm. The resulting "beams" diverge from the y direction with a maximum angle that varies slightly with energy (see Figure S5). In particular, when the tip injects into a ribbon site, this angle decreases from ~30° for $E - E_F < 0.3$ eV to ~20° for $0.4 < E - E_F < 0.8$ eV. We observe similar results for injection into a bridge site, although the interference in this case is more blurred because the injected currents start out by propagation in the two bridged ribbons (see Figure S2). We also find that the application of a finite bias voltage between the tip and the NPG does not disrupt the interference pattern (see Figure S6).

The Talbot interference generally refers to repeated self-imaging of a diffraction grating.[20] In this context, the wave amplitude, ψ_n, inside the nth element of an infinite array of weakly coupled discrete channels aligned along y obeys the following discrete differential equation[21,39−41]

$$i\frac{d\psi_n}{dy}(y) + \kappa_c[\psi_{n-1}(y) + \psi_{n+1}(y)] = 0 \quad (2)$$

where κ_c represents the interchannel coupling coefficient. The coefficient κ_c can be regarded as a figure-of-merit for the degree of 1D confinement in the elements of the array: The lower the value of κ_c, the lower the spread into the weakly coupled adjacent channels. In the particular case when only a single channel is initially excited, that is, $\psi_{n=0} = \psi_0$, the solutions for eq 2 can be written as[24,39,41]

$$\psi_n(y) = \psi_0 i^n J_n(2\kappa_c y) \quad (3)$$

where J_n is the Bessel function of the nth order.

We find that the square modulus of eq 3 can be fitted to the far-field spectral density of states originating from the tip. The best fit on a set of 53 channels of a 100 nm × 120 nm n-doped NPG is illustrated in Figure 2d. The fitted values at $E = 0.2$ eV are $\psi_0 = 0.037$ and $\kappa_c = 0.012$ Å^{-1}. The latter varies slightly within the energy range spanned by the first two longitudinal bands, as shown in Figure 3a,b.

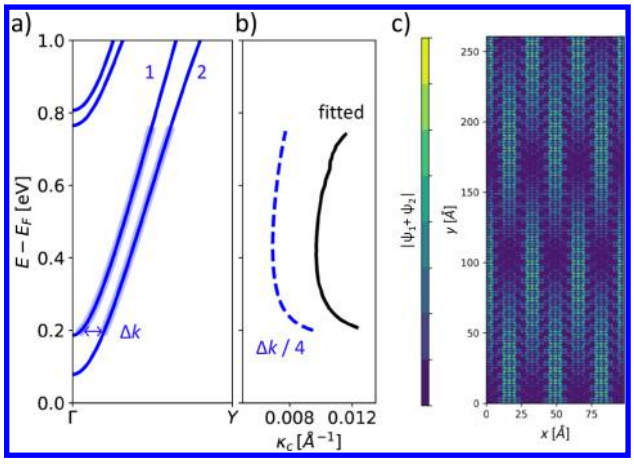

Figure 3. Origin of Talbot effect. (a) Longitudinal bands from a p_z TB model of n-doped NPG parametrized from DFT. (b) Energy dependence of inter-GNR coupling κ_c from fit to the Talbot eq 3 in comparison with $\Delta k/4 = |k_2 - k_1|/4$. (c) Amplitude of $\psi_1 + \psi_2$ at $E - E_F = 0.2$ eV, showing the interference underlying the Talbot effect.

The Talbot effect originates due to interference of the two longitudinal Bloch states ψ_1 and ψ_2. From the momentum difference, one can estimate the coupling strength as $\kappa_c = \Delta k/4 = |k_2 - k_1|/4$.[23,24] In Figure 3c, we plot $|\psi_1 + \psi_2|$ for the NPG without tip contact, showing the regular interference pattern expected when all GNRs are simultaneously excited.[23]

The latest developments in STM have enabled measurements with up to four tips[42] and control over tip−tip distance down to tens of nanometers.[18] Within this context, we propose to use dual-probe STM to reveal the electronic Talbot effect experimentally. One probe can be used to inject current into the NPG at a fixed position, as discussed above, whereas the second probe is used to map out the interference pattern. The tips are in chemical contact with the NPG rather than in the tunneling regime to maximize the current, important for the experimental feasibility. We use the modular capability of the multiscale approach to embed two DFT-precision tips in the large TB model. Both tips are located ~2 Å above NPG, and we fix the probe-tip distance to ~30 nm from the source. The probe-tip is moved between the bridge and ribbon positions

DOI: 10.1021/acs.nanolett.8b04616
Nano Lett. 2019, 19, 576−581

along the white line shown in the inset in Figure 4a. The calculated transmission between the two tips, injecting

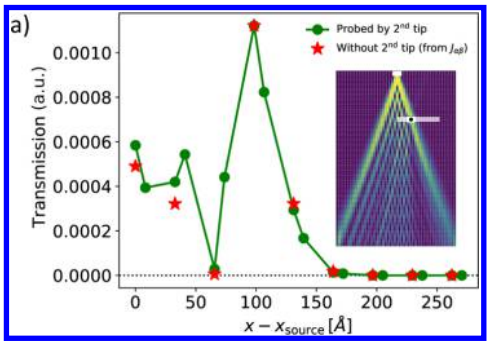

Figure 4. Probing the Talbot effect. (a) Transmission at $E - E_F = 0.2$ eV (green) measured by a second DFT-precision tip probing ribbon and bridge sites of *n*-doped NPG along the white line shown in the inset in comparison with bond currents flowing in the absence of the second tip (red). These are obtained on a "per ribbon" basis by summing all bond currents passing through the white line, without distinction between ribbon and bridge sites, and then scaling by a factor 1/16. The inset shows bond currents injected into the NPG (with same size as in Figure 2c) and scattering off the second tip for one of the scanned positions, indicated by the black dot.

electrons at $E - E_F = 0.2$ eV into *n*-doped NPG, is shown in Figure 4a. The maxima of transmission reproduce the maxima of bond currents injected from the source in the absence of the second tip within 5%. This proves that the signal in electric current detected by the second tip can map out the Talbot interference pattern. This also indicates that modifications of the NPG atomic structure and electron density due to the chemical contact with the tip do not suppress the effect. That being said, we speculate that evidence of the Talbot effect in NPG may be obtained by devising other types of experiments.

In conclusion, we have explored how electrons injected by an STM probe in chemical contact to gated NPG-based devices behave in near- and far-field. By performing multiscale parameter-free calculations of large-scale TB models of NPG with DFT-precision regions, we found a clear signature of phase-coherent electron waves, manifested in the far field as a Talbot interference effect. The origin of this phenomenon is the cross-talk between longitudinal 1D channels (GNRs) making up the NPG. Using proof-of-principle multiprobe calculations, we have shown that this interference effect may be observed in a dual-probe STM experiment.

Further investigations could potentially shed light on the important impact of defects, substrate, or pore functionalization on the current flow. Importantly, the chemical design of the inter-ribbon bridges could allow fine-tuning of the coupling strength, κ_c, to improve 1D transport confinement. We also speculate that the Talbot effect could be observed in other structures featuring weakly coupled quasi-1D channels, such as other anisotropic 2D materials[43−47] or crystals hosting surface states.[48] This effect in elastic, phase-coherent transport may be used to gain insights into the phase-breaking length in these structures due to various scattering mechanisms such as electron−phonon coupling. Finally, since topologically nontrivial states were found at the edges of chiral GNRs,[49,50] further studies may potentially reveal whether topological signatures could emerge in NPGs.

■ ASSOCIATED CONTENT

Supporting Information

The Supporting Information is available free of charge on the ACS Publications website at DOI: 10.1021/acs.nanolett.8b04616.

Computational details, DFT potential and charge distributions in gated NPG+tip systems, transmission and near-field bond currents from tip to DFT-modeled NPG, multiscale method applied to NPG+tip systems, transmission and far-field bond currents from DFT-precision tip to TB-modeled NPG, and bond-current maps from dual-probe calculations (PDF)

■ AUTHOR INFORMATION

Corresponding Authors

*G.C.: E-mail: gaca@nanotech.dtu.dk. Tel: +4591198180.
*M.B.: E-mail: mads.brandbyge@nanotech.dtu.dk. Tel: +4545256328.

ORCID

Gaetano Calogero: 0000-0003-3610-3231
Nick R. Papior: 0000-0003-3038-1855
Bernhard Kretz: 0000-0002-6728-1025
Aran Garcia-Lekue: 0000-0001-5556-0898
Mads Brandbyge: 0000-0002-0126-9824

Notes

The authors declare no competing financial interest.

■ ACKNOWLEDGMENTS

Financial support by Villum Fonden (00013340), Danish research council (4184-00030), Spanish Ministerio de Economía y Competitividad (FIS2017-83780-P and MAT2016-78293-C6-4-R), and UPV/EHU (IT-756-13) is gratefully acknowledged. The Center for Nanostructured Graphene (CNG) is sponsored by the Danish Research Foundation (DNRF103). We are thankful to Sidsel R. Papior, José Caridad, Pedro Brandimarte, Isaac Alcón Rovira, and Stephen Power for useful discussions.

■ REFERENCES

(1) Chen, L.; Zhang, Y.; Chen, G.; Franco, I. Stark control of electrons along nanojunctions. *Nat. Commun.* **2018**, *9*, 2070.
(2) Biele, R.; Rodríguez-Rosario, C. A.; Frauenheim, T.; Rubio, A. Controlling heat and particle currents in nanodevices by quantum observation. *npj Quantum Mater.* **2017**, *2*, 38.
(3) Karra, M.; Sharma, K.; Friedrich, B.; Kais, S.; Herschbach, D. Prospects for quantum computing with an array of ultracold polar paramagnetic molecules. *J. Chem. Phys.* **2016**, *144*, 094301.
(4) Prindle, A.; Samayoa, P.; Razinkov, I.; Danino, T.; Tsimring, L. S.; Hasty, J. A sensing array of radically coupled genetic 'biopixels'. *Nature* **2012**, *481*, 39.
(5) Brandimarte, P.; Engelund, M.; Papior, N.; Garcia-Lekue, A.; Frederiksen, T.; Sánchez-Portal, D. A tunable electronic beam splitter realized with crossed graphene nanoribbons. *J. Chem. Phys.* **2017**, *146*, 092318.
(6) Pedersen, T. G.; Flindt, C.; Pedersen, J.; Mortensen, N. A.; Jauho, A.-P.; Pedersen, K. Graphene Antidot Lattices: Designed Defects and Spin Qubits. *Phys. Rev. Lett.* **2008**, *100*, 136804.
(7) Bai, J.; Zhong, X.; Jiang, S.; Huang, Y.; Duan, X. Graphene nanomesh. *Nat. Nanotechnol.* **2010**, *5*, 190.
(8) Moreno, C.; Vilas-Varela, M.; Kretz, B.; Garcia-Lekue, A.; Costache, M. V.; Paradinas, M.; Panighel, M.; Ceballos, G.; Valenzuela, S. O.; Peña, D.; Mugarza, A. Bottom-up synthesis of multifunctional nanoporous graphene. *Science* **2018**, *360*, 199−203.

DOI: 10.1021/acs.nanolett.8b04616
Nano Lett. 2019, 19, 576−581

(9) Caridad, J. M.; Calogero, G.; Pedrinazzi, P.; Santos, J. E.; Impellizzeri, A.; Gunst, T.; Booth, T. J.; Sordan, R.; Bøggild, P.; Brandbyge, M. A Graphene-Edge Ferroelectric Molecular Switch. *Nano Lett.* **2018**, *18*, 4675−4683.
(10) Chen, S.; Han, Z.; Elahi, M. M.; Habib, K. M. M.; Wang, L.; Wen, B.; Gao, Y.; Taniguchi, T.; Watanabe, K.; Hone, J.; Ghosh, A. W.; Dean, C. R. Electron optics with p−n junctions in ballistic graphene. *Science* **2016**, *353*, 1522−1525.
(11) Caridad, J. M.; Connaughton, S.; Ott, C.; Weber, H. B.; Krstić, V. An electrical analogy to Mie scattering. *Nat. Commun.* **2016**, *7*, 12894.
(12) Bøggild, P.; Caridad, J. M.; Stampfer, C.; Calogero, G.; Papior, N. R.; Brandbyge, M. A two-dimensional Dirac fermion microscope. *Nat. Commun.* **2017**, *8*, 15783.
(13) Xu, H. Y.; Wang, G. L.; Huang, L.; Lai, Y. C. Chaos in Dirac Electron Optics: Emergence of a Relativistic Quantum Chimera. *Phys. Rev. Lett.* **2018**, *120*, 124101.
(14) Allen, M. T.; Shtanko, O.; Fulga, I. C.; Akhmerov, A. R.; Watanabe, K.; Taniguchi, T.; Jarillo-Herrero, P.; Levitov, L. S.; Yacoby, A. Spatially resolved edge currents and guided-wave electronic states in graphene. *Nat. Phys.* **2016**, *12*, 128.
(15) Silveiro, I.; Ortega, J. M. P.; de Abajo, F. J. G. Quantum nonlocal effects in individual and interacting graphene nanoribbons. *Light: Sci. Appl.* **2015**, *4*, No. e241.
(16) Bhandari, S.; Lee, G.-H.; Klales, A.; Watanabe, K.; Taniguchi, T.; Heller, E.; Kim, P.; Westervelt, R. M. Imaging Cyclotron Orbits of Electrons in Graphene. *Nano Lett.* **2016**, *16*, 1690−1694.
(17) Tetienne, J. P.; Dontschuk, N.; Broadway, D. A.; Stacey, A.; Simpson, D. A.; Hollenberg, L. C. Quantum imaging of current flow in graphene. *Sci. Adv.* **2017**, *3*, No. e1602429.
(18) Kolmer, M.; Olszowski, P.; Zuzak, R.; Godlewski, S.; Joachim, C.; Szymonski, M. Two-probe STM experiments at the atomic level. *J. Phys.: Condens. Matter* **2017**, *29*, 444004.
(19) Talbot, H. F. LXXVI. Facts relating to optical science. no. IV. *Philos. Mag. (1798−1977)* **1836**, *9*, 401.
(20) Berry, M.; Marzoli, I.; Schleich, W. Quantum carpets, carpets of light. *Phys. World* **2001**, *14*, 39−44.
(21) Iwanow, R.; May-Arrioja, D. A.; Christodoulides, D. N.; Stegeman, G. I.; Min, Y.; Sohler, W. Discrete talbot effect in waveguide arrays. *Phys. Rev. Lett.* **2005**, *95*, 053902.
(22) Chen, Z.; Zhang, Y.; Xiao, M. Discrete Talbot effect in two-dimensional waveguide arrays. *Opt. Express* **2015**, *23*, 14724.
(23) Walls, J. D.; Hadad, D. The talbot effect for two-dimensional massless Dirac fermions. *Sci. Rep.* **2016**, *6*, 1−11.
(24) Wang, L.; Jia, Y.; Ji, Z. Discrete plasmonic Talbot effect in single-mode graphene ribbon arrays. *Appl. Opt.* **2017**, *56*, 9998−10002.
(25) Solak, H.; Dais, C.; Clube, F. Displacement Talbot lithography: a new method for high-resolution patterning of large areas. *Opt. Express* **2011**, *19*, 10686−10691.
(26) Birnbacher, L.; Willner, M.; Velroyen, A.; Marschner, M.; Hipp, A.; Meiser, J.; Koch, F.; Schröter, T.; Kunka, D.; Mohr, J.; Pfeiffer, F.; Herzen, J. Experimental Realisation of High-sensitivity Laboratory X-ray Grating-based Phase-contrast Computed Tomography. *Sci. Rep.* **2016**, *6*, 24022.
(27) Brandbyge, M.; Mozos, J.-L.; Ordejón, P.; Taylor, J.; Stokbro, K. Density-functional method for nonequilibrium electron transport. *Phys. Rev. B: Condens. Matter Mater. Phys.* **2002**, *65*, 165401.
(28) Datta, S. Nanoscale device modeling: the Green's function method. *Superlattices Microstruct.* **2000**, *28*, 253−278.
(29) Saha, K. K.; Nikolić, B. K.; Meunier, V.; Lu, W.; Bernholc, J. Quantum-Interference-Controlled Three-Terminal Molecular Transistors Based on a Single Ring-Shaped Molecule Connected to Graphene Nanoribbon Electrodes. *Phys. Rev. Lett.* **2010**, *105*, 236803.
(30) Soler, J. M.; Artacho, E.; Gale, J. D.; García, A.; Junquera, J.; Ordejón, P.; Sánchez-Portal, D. The SIESTA method for ab initio order-N materials simulation. *J. Phys.: Condens. Matter* **2002**, *14*, 2745−2779.
(31) Papior, N.; Lorente, N.; Frederiksen, T.; García, A.; Brandbyge, M. Improvements on non-equilibrium and transport Green function techniques: The next-generation transiesta. *Comput. Phys. Commun.* **2017**, *212*, 8−24.
(32) Papior, N. R. *sisl*, version 0.9.5, 2018.https://github.com/zerothi/sisl.
(33) Papior, N. R.; Calogero, G.; Brandbyge, M. Simple and efficient LCAO basis sets for the diffuse states in carbon nanostructures. *J. Phys.: Condens. Matter* **2018**, *30*, 25LT01.
(34) Perdew, J. P.; Burke, K.; Ernzerhof, M. Generalized Gradient Approximation Made Simple. *Phys. Rev. Lett.* **1996**, *77*, 3865−3868.
(35) Papior, N.; Gunst, T.; Stradi, D.; Brandbyge, M. Manipulating the voltage drop in graphene nanojunctions using a gate potential. *Phys. Chem. Chem. Phys.* **2016**, *18*, 1025.
(36) Paulsson, M.; Brandbyge, M. Transmission eigenchannels from nonequilibrium Green's functions. *Phys. Rev. B: Condens. Matter Mater. Phys.* **2007**, *76*, 115117.
(37) Calogero, G.; Papior, R. N.; Bøggild, P.; Brandbyge, M. Large-scale tight-binding simulations of quantum transport in ballistic graphene. *J. Phys.: Condens. Matter* **2018**, *30*, 364001.
(38) Xie, H.; Kwok, Y.; Jiang, F.; Zheng, X.; Chen, G. Complex absorbing potential based Lorentzian fitting scheme and time dependent quantum transport. *J. Chem. Phys.* **2014**, *141*, 164122.
(39) Yariv, A.; Yeh, P. *Optical Waves in Crystals: Propagation and Control of Laser Radiation*; Wiley Series in Pure and Applied Optics; Wiley-Interscience: New York, 1984.
(40) Pertsch, T.; Zentgraf, T.; Peschel, U.; Bräuer, A.; Lederer, F. Anomalous refraction and diffraction in discrete optical systems. *Phys. Rev. Lett.* **2002**, *88*, 093901.
(41) Somekh, S.; Garmire, E.; Yariv, A.; Garvin, H. L.; Hunsperger, R. G. Channel optical waveguide directional couplers. *Appl. Phys. Lett.* **1973**, *22*, 46−47.
(42) Baringhaus, J.; Settnes, M.; Aprojanz, J.; Power, S. R.; Jauho, A. P.; Tegenkamp, C. Electron Interference in Ballistic Graphene Nanoconstrictions. *Phys. Rev. Lett.* **2016**, *116*, 186602.
(43) Lv, Y.; Chang, S.; Huang, Q.; Wang, H.; He, J. Scaling effect of phosphorene nanoribbon - Uncovering the origin of asymmetric current transport. *Sci. Rep.* **2016**, *6*, 38009.
(44) Kou, L.; Frauenheim, T.; Chen, C. Phosphorene as a Superior Gas Sensor: Selective Adsorption and Distinct I-V Response. *J. Phys. Chem. Lett.* **2014**, *5*, 2675−2681.
(45) Xia, F.; Wang, H.; Jia, Y. Rediscovering black phosphorus as an anisotropic layered material for optoelectronics and electronics. *Nat. Commun.* **2014**, *5*, 4458.
(46) Mannix, A. J.; Zhou, X.-F.; Kiraly, B.; Wood, J. D.; Alducin, D.; Myers, B. D.; Liu, X.; Fisher, B. L.; Santiago, U.; Guest, J. R.; Yacaman, M. J.; Ponce, A.; Oganov, A. R.; Hersam, M. C.; Guisinger, N. P. Synthesis of borophenes: Anisotropic, two-dimensional boron polymorphs. *Science* **2015**, *350*, 1513−1516.
(47) An, Y.; Jiao, J.; Hou, Y.; Wang, H.; Wu, D.; Wang, T.; Fu, Z.; Xu, G.; Wu, R. How does the electric current propagate through fully-hydrogenated borophene? *Phys. Chem. Chem. Phys.* **2018**, *20*, 21552−21556.
(48) Engelund, M.; Papior, N.; Brandimarte, P.; Frederiksen, T.; Garcia-Lekue, A.; Sánchez-Portal, D. Search for a Metallic Dangling-Bond Wire on n-Doped H-Passivated Semiconductor Surfaces. *J. Phys. Chem. C* **2016**, *120*, 20303−20309.
(49) Gröning, O.; Wang, S.; Yao, X.; Pignedoli, C. A.; Borin Barin, G.; Daniels, C.; Cupo, A.; Meunier, V.; Feng, X.; Narita, A.; Müllen, K.; Ruffieux, P.; Fasel, R. Engineering of robust topological quantum phases in graphene nanoribbons. *Nature* **2018**, *560*, 209−213.
(50) Rizzo, D. J.; Veber, G.; Cao, T.; Bronner, C.; Chen, T.; Zhao, F.; Rodriguez, H.; Louie, S. G.; Crommie, M. F.; Fischer, F. R. Topological Band Engineering of Graphene Nanoribbons. *Nature* **2018**, *560*, 204−208.

DOI: 10.1021/acs.nanolett.8b04616
Nano Lett. 2019, 19, 576−581